Research Square

Preprints are preliminary reports that have not undergone peer review.
They should not be considered conclusive, used to inform clinical practice,
or referenced by the media as validated information.

Phase-Cone Biomarkers Derived from Microgrid ECoG and Its Temporal Derivatives During Seizure Evolution and Reading

Ceon Ramon

ceon@uw.edu

University of Washington

Alex Doud

University of Washington

Shahin Hakimian

University of Washington

Nicholas Poolos

University of Washington

Research Article

Keywords: Phase cones, microgrid ECoG, seizure dynamics, cortical phase transitions, EEG time-series analysis, micro-electrocorticography (μECoG), metastability

Posted Date: November 6th, 2026

DOI: https://doi.org/10.21203/rs.3.rs-11320855/v1

License: This work is licensed under a Creative Commons Attribution 4.0 International License.
Read Full License

Additional Declarations: No competing interests reported.

Abstract

EEG and micro-electrocorticographic (μECoG) recordings exhibit transient spatiotemporal phase-cone structures that are thought to reflect cortical phase transitions underlying cognitive processing and epileptic activity. In this study, we investigated phase-cone dynamics in human micro-electrocorticographic (μECoG) recordings obtained from an 8 × 8 cortical microgrid implanted near a seizure onset zone. Phase-cone rates (PCRs) were computed from the original signal (PCR1), its first temporal derivative (PCR2), and its second temporal derivative (PCR3) in theta (4–8 Hz), alpha (8–12 Hz), beta (12–30 Hz), and low-gamma (30–50 Hz) frequency bands during an evolving focal seizure and a normal reading task. All three PCR measures exhibited a robust spectral hierarchy, increasing progressively from theta to low-gamma frequencies. During a reading task, PCR activity was relatively stable and showed modest temporal fluctuations consistent with ongoing cortical state transitions. In contrast, seizure activity produced substantially larger PCR magnitudes and greater temporal variability, particularly in the beta and low-gamma bands, indicating enhanced phase-transition dynamics during ictal network evolution. Analysis of temporally differentiated signals demonstrated that organized phase-cone structures remain detectable after first- and second-order differentiation, suggesting that cortical state transitions are reflected not only in instantaneous phase patterns but also in their temporal rates of change. These findings indicate that phase-cone dynamics are preserved across multiple dynamical representations of cortical activity and support the use of derivative-based PCR measures as complementary biomarkers of mesoscopic cortical organization. The proposed framework may provide new insights into normal cognitive processing, seizure dynamics, and other conditions involving large-scale cortical reorganization.

1. Introduction

This paper is dedicated to the centennial celebration of Walter J. Freeman, III, honoring his pioneering contributions to the study of mass action in the nervous system, and the formation of stabilizing vortices in brain waves (Freeman 1975; Freeman et al. 2006a; Freeman and Vitiello 2006; Ruiz et al. 2010; Kozma 2016; Kozma and Freeman 2017). Concurrently, we commemorate the life and work of our late colleague at the University of Washington, Mark D. Holmes. For nearly three decades (1988–2016), Dr. Holmes collaborated closely with Professor Freeman, investigating cortical phase transitions, scale-free self-organized criticality, and the tracking of high-density phase cone structures within the electroencephalogram (EEG) of both healthy individuals and patients with epilepsy (Freeman 2004; Freeman et al. 2003; Freeman and Holmes 2005; Freeman et al. 2006b; Ramon et al. 2008, 2009, 2013, 2018).

The present work extends our previous study (Ramon et al. 2024), which investigated phase slip rates and instantaneous phase cones derived exclusively from the time-series data, y(t), of human micro-electrocorticography (micro-ECoG or μECoG). Here, we expand this framework to examine the stable formation of phase cones using not only the raw signal, but also its first-order (y'(t) = dy/dt) and second-order (y"(t) = dy'/dt) derivatives. This approach builds on recent findings indicating that phase slip rates

extracted from the derivatives of electrophysiological data provide deeper insights into cortical phase transitions, thereby enhancing our capacity to map micro-dynamics during both cognitive tasks and epileptogenic activity (Ramon et al. 2023; Ramon and Gargiulo 2025). Importantly, this study serves primarily as a methodological development paper aimed at engineering and evaluating these advanced spatiotemporal biomarkers, rather than a large-scale clinical validation trial. Consequently, we apply and test these novel mathematical tools using a high-density microgrid ECoG dataset from a single subject.

This specific dataset was selected for two primary reasons. First, it was originally collected by Walter J. Freeman, Mark Holmes, and their team (Freeman et al. 2006a, b; Panagiotides et al. 2011), whose centennial legacy this work honors. Second, as a high-density subdural microgrid dataset, it is free from physiological contamination, such as myogenic, cardiac, and ocular artifacts, making it an ideal benchmark dataset for evaluating novel spatiotemporal biomarkers. Further technical specifications of this dataset are detailed in the Methods section. By utilizing this artifact-free recording, we establish a controlled computational environment to rigorously demonstrate the feasibility and analytical behavior of derivative-based phase cone formations. Ultimately, these advanced mathematical biomarkers hold the potential for broad application across diverse modalities of clinical and cognitive neuroimaging datasets in future large-cohort investigations.

2. Background Material

The spatiotemporal dynamics of the human cortex are characterized by a continuous, cinematic cycle of self-organized state changes, which are captured via electroencephalogram (EEG) recordings as cortical phase transitions (Freeman et al. 2006a; Kozma and Freeman 2017; Freeman and Quiroga 2013). In healthy cognitive processing, neural populations optimize computational flexibility by remaining near a state of self-organized criticality (Thatcher et al. 2009), rapidly alternating between ordered synchronization and sudden, functional intervals of disorder, sometimes conceptualized as phase resets (Thatcher et al. 2014; Freeman and Holmes 2005; Ramon and Gargiulo 2025). The emergence of highly synchronized, large-scale amplitude modulation (AM) patterns represents stable perceptual "frames" of conscious thought (Ruiz et al. 2010). Crucially, the termination of these frames is mediated by sharp phase slips, or desynchronization events, where the robust coordination abruptly collapses, resetting the neural populations back into an asynchronous background state (Ramon et al. 2008). This transition from order to disorder serves as an essential "shutter" that clears the cortical canvas, preparing the network to build the next cognitive frame (Panagiotides et al. 2011).

In clinical pathology, however, particularly in patients with epilepsy, this delicate balance between order and chaotic disorder becomes severely compromised. High-density scalp EEG and microgrid recordings demonstrate that instead of transitioning fluidly through desynchronized intervals, the epileptic cortex displays a significant deceleration in phase slip rates and a collapse of localized phase cone structures (Ramon and Holmes 2020). This lack of disordered phase slips implies that the pathological network loses its capacity to reset, allowing massive populations of neurons to escape their flexible baseline state and lock into rigid, hyper-synchronous ictal configurations (Freeman et al. 2006b; Ramon et al.

2018). This is what Freeman's theoretical and experimental work predicted, and stable phase slips and phase cone formations may decrease during ictal periods near the start of a seizure, as well as during seizure evolution. Our results confirm Freeman's predictions: during seizure evolution, the rate of stable phase cone formation decreases. In addition, we show that stable-phase cones oscillate during cognitive tasks, such as reading, and differ from seizure evolution. For this, we used μECoG data from the same subject during a reading task performed during an interictal period (Panagiotides et al. 2011).

2.1 Phase Slips and Phase Cone Formations

Cortical phase transitions manifest as brief bursts of collective neural activity, appearing as small spatiotemporal perturbations in electroencephalogram (EEG) or micro-electrocorticography (μECoG) traces. The underlying analytic phase can be formally extracted by applying the Hilbert transform to the bandpass-filtered electrophysiological data (Freeman et al. 2006a; Ramon et al. 2024). Following phase unwrapping and detrending, sharp phase slips, representing abrupt desynchronization events, become visible at the exact temporal locations of perturbations in the μECoG signal. These phase slips can occur isolated at a single electrode or simultaneously across an array of nearby channels.

Under specific physiological conditions, a cluster of synchronized phase slips across adjacent electrodes can form organized spatial topographies known as phase cones (Freeman et al. 2006a; Ruiz et al. 2010; Kozma and Freeman 2017; Myers et al. 2014). While both phase slips and phase cones serve as highly sensitive biomarkers of cortical state changes (Ramon et al. 2024), spatial phase cones potentially offer superior diagnostic sensitivity. This heightened sensitivity stems from their structural prerequisites, which require both the simultaneous occurrence of localized phase slips and the preservation of strict spatial phase gradients across neighboring cortical sites (Ramon et al. 2018; Ramon and Holmes 2020). In our previous work, we examined the distinct dynamics of phase slip rates and instantaneous phase cones during seizure evolution using human μECoG data. The present study extends that framework to evaluate the stable, derivative-based formation of phase cones during both epileptic seizure propagation and the cognitive task of reading.

The technical specifications of the μECoG dataset, alongside the mathematical procedures used to extract phase profiles and calculate stable phase-cone rates (PCRs), are detailed in the Methods section. The Results section provides a comprehensive spatiotemporal analysis of PCR dynamics during ictal activity and cognitive processing. Finally, a critical evaluation of these methodological developments, their clinical implications, and the limitations of this study are presented in the Discussion section.

3. Methods

3.1 μECoG Data

Comprehensive details regarding this dataset are provided in prior studies (Freeman et al. 2006a, 2006b; Panagiotides et al. 2011; Ramon et al. 2024). For completeness, we summarize the key parameters here.

The subject, a 34-year-old woman with refractory focal impaired awareness seizures, underwent preoperative evaluation at the Harborview Medical Center Epilepsy Center (University of Washington, Seattle). Localization of the seizure onset zone was established using standard intracranial subdural strip electrodes placed over the lateral and basal-temporal regions. Additionally, after IRB approval and informed consent, an 8 × 8 microgrid (1×1 cm, 1.25 mm interelectrode spacing) was placed on the right inferior temporal gyrus near the onset zone (Fig. 1A). The patient remained seizure-free after surgery. Figure 1A shows the skull X-ray with a white circle marking the microgrid location (left) and, on the right, a layout of the electrodes on an 8 × 8 microgrid. The electrodes are marked horizontally, starting with #1 at the top-left corner. Some other electrodes, e.g., #8, #28, and #57, are also marked for easier identification. More details about the other panels in Fig. 1 are described later on in this section.

Continuous video-EEG recording was conducted over eight days, during which various motor and non-motor epileptogenic events occurred. For the current phase cone analysis, we selected one artifact-free, long-duration seizure (~ 100 s). This specific event was characterized by progressive cognitive decline, including confusion, anxiety, and slowed thinking without motor symptoms. Electrographic onset preceded clinical manifestations by approximately 10 seconds.

In addition, for comparative analysis, we used approximately 10 min of interictal data collected during a cognitive reading task, at least 2 hours away from any seizure activity (Freeman et al. 2006b). From these 10 min of data, we randomly selected a 100-s segment for phase-cone analysis during the interictal period and compared these results with those derived from seizure data of the same duration (100 s).

An example of the acquired dataset is presented in Fig. 1, illustrating a 5-second continuous segment recorded during an ictal state (Fig. 1B) alongside a baseline cognitive state (Fig. 1C) captured while the subject was actively engaged in a reading task. Cortical signals were collected utilizing an 8×8 microgrid array; for clarity, only 8 channels corresponding to the fourth electrode row are plotted here. The power spectral densities (PSDs) calculated across all eight combined channels are detailed in Fig. 1D. Visually, ictal data (Panel B) shows a significantly lower and highly regular repetition frequency, with approximately 3 to 4 prominent wave cycles within each 1-second interval. Conversely, interictal data (Panel C) during the reading task shows a markedly higher, desynchronized frequency profile, visible as dense, rapid micro-oscillations with numerous compressed sub-cycles within the same 1-second window. Quantitative spectral analysis (panel D) highlights these distinct frequency characteristics between the two behavioral states. Ictal activity in Panel B is dominated by the theta band (3–7 Hz) and delta band (< 3 Hz), reflecting pathological, hypersynchronous slow-wave discharges. In contrast, these low-frequency rhythms are entirely suppressed during the reading task (Panel C). Instead, signal power shifts significantly toward higher frequencies, with the beta band (12–30 Hz) and low-gamma band (30–50 Hz) becoming prominent. This spectral shift signifies the localized, desynchronized cortical processing required for text comprehension and active visual attention, which occurs concurrently with the observed attenuation (blocking) of the resting alpha band (7–12 Hz).

3.2 Phase Cones Extraction and Phase-Cone Rate Computation

Several methods have been used to identify phase-cone structures in EEG recordings. Early studies detected phase cones by fitting conical surfaces to spatial distributions of analytic phase and estimating parameters such as cone diameter, duration, and propagation velocity (Freeman 2004). Later, probabilistic and optimization-based approaches were introduced to improve detection of transient phase-cone events in noisy EEG data (Myers et al. 2014). In our previous work, stable phase cones were identified by requiring a consistent phase-gradient sign for at least three consecutive time samples and propagation velocities compatible with known cortical conduction velocities (Ramon and Holmes 2020). Other investigators have used spatially smoothed phase-surface representations and stable phase-structure detection algorithms to facilitate the identification of propagating phase wave fronts and coherent phase patterns (Freeman 2004; Ruiz et al. 2008). The present study extends this geometric persistence approach to both the original μECoG signals and their first- and second-order temporal derivatives using a common set of detection criteria. This strategy preserves the native temporal resolution of the data, avoids introducing additional smoothing assumptions, and provides a consistent framework for comparing phase-transition dynamics across signal representations.

The original data, initially sampled at 200 Hz, was bandpass filtered within the given band, e.g., the alpha band (7–12 Hz), using a zero-phase, forward-backward finite impulse response (FIR) filter configured with 1 Hz transition boundaries and 60 dB stop-band attenuation. The data was referenced to the common averaged reference for each channel. To improve temporal fidelity and enable precise velocity profiling with axonal velocities (Innocenti et al. 2014), the signal was upsampled to 2000 Hz using the polyphase resample function in MATLAB; this method uses an integrated anti-aliasing low-pass filter, avoiding the sampling noise and interpolation artifacts typically inherent in cubic spline interpolation (Vaidyanathan, 1993). It has been previously suggested (Freeman and Kozma, 2010; Kozma and Freeman 2008; Kozma et al. 2005) that to map spatial geometries of mesoscopic wave packets (phase cones) an interelectrode spacing of 0.8 mm or less is needed. Also, to prevent spatial aliasing of the local field potentials and to match up with the axonal velocities of 1–10 mm/ms, a sampling with 0.2 ms time samples might be needed (Kozma et al. 2005; Freeman and Kozma 2010). Thus, upsampling in the spatial and temporal domains of the original μECoG data is needed to extract stable phase cones. More details about implementing these criteria are given later in this section.

The complex analytic signal for each upsampled channel was then extracted via the Hilbert transform, and the underlying phase trajectories were derived from the four-quadrant inverse tangent and continuously unwrapped over time to eliminate artificial 2π phase discontinuities. The phase frequencies in Hz (cycles/s) were computed by taking the derivatives of the unwrapped phase and dividing by 2π. To facilitate spatial analysis, these multi-channel frequency time series were mapped into an 8 × 8 topological tensor corresponding to the physical geometry of the electrode array.

To overcome discrete physical sampling constraints and resolve localized submillimeter phase gradients, the bounded spatial fields from each temporal frame were projected onto the complex unit circle using their Euler components. The real and imaginary components were independently upsampled to a 16 × 16 virtual sensor grid, corresponding to an effective spatial resolution of 0.625 mm, using two-dimensional bicubic-spline interpolation. The resulting fields were then smoothed with a 3 × 3 uniform spatial convolution to attenuate microscale jitter while preserving the circular topology of the phase representation.

Stable phase cones were identified using the following physiological criteria:

(1) The phase frequency fell within the specified frequency band, such as 7–12 Hz for the alpha band.

(2) The phase gradient across neighboring electrodes was consistently positive or negative.

(3). The gradient exceeded the 55% threshold for three consecutive temporal samples.

(4) The change in peak magnitude was less than 5% of the local mean across the same three consecutive samples.

(5) The estimated conduction velocity fell within 2 to 5 mm/ms.

The final criterion was selected based on the reported axonal conduction-velocity range of 1–10 mm/ms (Innocenti et al. 2014; Swadlow and Waxman 2012). At an upsampled sampling rate of 2000 Hz, the temporal interval between samples is 0.5 ms. Therefore, conduction velocities of 2–5 mm/ms correspond to travel distances of 1.0–2.5 mm between consecutive samples. This range supports the extraction of local phase-cone formations with base lengths of approximately 1.25 to 2.5 mm across adjacent 3 × 3 or 4 × 4 electrode neighborhoods on the 16 × 16 virtual sensor grid. The outermost electrodes of the virtual grid were excluded as candidates for the location of the apex of phase cones. Validated apices were classified into phase peaks (expanding wave sources) or valleys (contracting sinks) based on their 4-connected spatial neighborhood polarity.

The number of stable phase cones was computed at each time point. From these, PCRs were computed using a sliding window of 10 ms with a step size of 0.5 ms, corresponding to one digitization point at an upsampled rate of 2000 Hz. This 10 ms window was chosen to cover half a wavelength of the highest frequency of interest (50 Hz). The resulting PCR profile was then downsampled to the original sampling rate of 200 Hz, and a smoothing spline curve was fitted to obtain the final temporal profile. PCRs were computed from y(t), y'(t), and y"(t), designated as PCR1, PCR2, and PCR3, respectively. The units are expressed as counts per 10 ms, reflecting the duration of the sliding window. This analysis was performed across the theta (3–7 Hz), alpha (7–12 Hz), beta (12–30 Hz), and low-gamma (30–50 Hz) frequency bands.

3.3 Phase-Cones in Randomized Data

The above analysis was also performed on the randomized data and its derivatives.

For random-data testing, the upsampled 8 × 8 μECoG data were first temporally shuffled by randomly permuting (Lancaster 2018) the sample order across all channels, preserving the channel-wise amplitude distribution while removing time structure. Each shuffled realization was then screened for a white-noise-like power spectrum using Welch PSD estimates computed after mean subtraction on each channel. A spectral flatness index and the channel-averaged PSD spread in dB were used as the whiteness criteria, with acceptance requiring flatness > = 0.85 and spread < = 3.0 dB. If a shuffled realization failed this criterion, zero-mean white Gaussian noise was added iteratively, starting at 0.02 times the signal standard deviation and doubling each round up to a maximum of 0.25, with up to four noise-injection rounds permitted. The resulting surrogate data were then transformed with the Hilbert method to obtain instantaneous phase, reshaped into an 8 × 8 grid, and passed through the same phase-cone detection pipeline as the original data. The mean number of active cones over time was used as the trial-level summary statistic across 1000 Monte Carlo realizations. It was found that stable phase cones and associated PCRs were zero in all the bands for 1000 trials. This shows that our reported results reflect biological processes that give rise to coordinated cortical neuronal activity and are above random noise.

3.4 Significance Analysis

PCR values from theta, alpha, beta, and low-gamma bands were analyzed as the primary outcome. To reduce autocorrelation, the PCR time series were averaged into non-overlapping 1-s windows. Descriptive statistics were computed for each band. Band differences were tested with repeated-measures ANOVA and confirmed with a Friedman test when applicable. Post hoc pairwise comparisons were Bonferroni-corrected. Effect sizes were reported as partial eta squared, η, for the omnibus ANOVA and paired Cohen's dz for pairwise comparisons. The effect size based on Cohen’s d (Brydges 2019; Cohen 1992) were classified as: d = 0.20, 0.50, and 0.80 to be interpreted as small, medium, or large, respectively. The effect size based on partial eta squared (η) are classified (Richardson 2011) as: small ($\eta < 0.06$), moderate ($0.06 \leq \eta < 0.14$), and large ($\eta \geq 0.14$).

3.5 Software and Computational resources

MATLAB and EEGLAB were used for data analysis. All analysis scripts were developed by our team for this project with assistance from MATLAB Copilot, which is integrated into MATLAB. Each script was manually reviewed line by line to verify its correctness, ensure that the code accurately reflected the underlying mathematical principles, and prevent blind reliance on MATLAB Copilot. The analyses were conducted on a desktop computer equipped with 128 GB of memory and an Intel® Core™ Ultra 9 processor operating at 2.50 GHz with 24 cores.

4. Results

4.1 PCR Activity during Seizure Evolution

Figure 2A illustrates the temporal evolution of ictal μECoG activity recorded from electrode #28, together with phase-cone rates (PCRs) in four frequency bands (Fig. 2B–E) over an approximately 100-s recording epoch. The band-limited μECoG signal (3–50 Hz; Fig. 2A) exhibits relatively low-amplitude activity during the initial portion of the epoch, followed by a progressive increase in amplitude and signal variability beginning at approximately 50 s and becoming most pronounced between 60 and 100 s, consistent with the development and intensification of seizure activity. PCRs in the theta (3–7 Hz), alpha (7–12 Hz), beta (12–30 Hz), and low-gamma (30–50 Hz) bands are characterized by intermittent transient elevations rather than sustained increases. PCR1 (blue), PCR2 (black), and PCR3 (red) exhibit distinct temporal and frequency-dependent dynamics. In the theta and alpha bands, PCR1 displays prominent fluctuations and transient elevations during the early (0–50 s) and intermediate (50–70 s) portions of the recording, whereas PCR2 remains comparatively low, with localized increases at later time points. In the beta and low-gamma bands, PCR1 is most pronounced during the early-to-intermediate interval and subsequently decreases. PCR2 and PCR3 exhibit more intermittent activity, including late PCR3 elevations in the low-gamma band. Overall, these results demonstrate temporally heterogeneous and frequency-specific phase-cone dynamics that do not simply mirror the amplitude evolution of the ictal μECoG signal, suggesting frequency-dependent changes in organized phase interactions during seizure development and progression.

Figure 2 does not show the detailed behavior of PCR activity. A detailed view of a 20-s segment is given in Fig. 3. In the theta band, PCR1 shows a pronounced decline during this interval, despite continued fluctuations in the underlying μECoG signal. This reduction is temporally distinct from the more intermittent activity of PCR2 and PCR3, which exhibit localized increases later in the segment. The alpha-, beta-, and low-gamma-band PCRs also display band-specific transients, including intermittent elevations of PCR2 and PCR3, but do not show an equivalent sustained reduction in PCR1. These observations highlight the finer temporal resolution of PCR measures and suggest that phase-cone dynamics can reveal transient, frequency-specific changes in ictal network organization that are not readily apparent from broadband μECoG amplitude alone.

PCR1 showed clear frequency-dependent variation across the four bands. Mean PCR1 values increased from 11.91 ± 5.81 in the theta band to 18.74 ± 12.83 in the alpha band, 26.18 ± 15.04 in the beta band, and 26.88 ± 11.99 in the low-gamma band. A repeated-measures ANOVA revealed a significant main effect of frequency band, $F(3, 291) = 67.26$, $p < 0.001$. This effect remained significant after Greenhouse–Geisser correction ($p < 0.001$). The corresponding effect size, calculated from the reported sums of squares, was substantial (partial eta squared approximately, $\eta = 0.41$). Bonferroni-adjusted pairwise comparisons showed significantly higher PCR1 values in the alpha, beta, and low-gamma bands than in the theta band, as well as higher values in the beta and low-gamma bands than in the alpha band (all adjusted $p < .001$). The beta and low-gamma bands did not differ significantly ($p < 1.00$). Consistent with these findings, the Friedman test also demonstrated a significant overall effect of frequency band, (3) = 104.89, $p < 0.001$. Its post hoc comparisons identified significant differences between theta and beta, theta and low-gamma, alpha and beta, and alpha and low-gamma, whereas the theta-versus-alpha and beta-versus-low-gamma comparisons were not significant. PCR1 values were strongly correlated

between the alpha and beta bands (r = 0.858) and moderately correlated between the beta and low-gamma bands (r = 0.602), while weaker associations were observed among the remaining band pairs.

PCR2 showed a progressive increase in activity across the frequency bands. Mean PCR2 values increased from 3.38 ± 2.34 in the theta band to 7.26 ± 4.73 in the alpha band, 13.17 ± 5.07 in the beta band, and 23.13 ± 8.24 in the low-gamma band. A repeated-measures ANOVA revealed a highly significant main effect of frequency band, $F(3, 291) = 361.44$, $p < 0.01$. This effect remained significant after Greenhouse–Geisser correction ($p < 0.001$) and was associated with a large effect size (partial eta squared approximately 0.79, calculated from the reported sums of squares). Bonferroni-adjusted pairwise comparisons showed that PCR2 differed significantly between all frequency bands, with values increasing successively from theta to alpha, beta, and low-gamma (all adjusted $p < .001$). Consistent with the parametric analysis, the Friedman test demonstrated a significant overall effect of frequency band, $\chi2(3) = 261.16$, $p < 0.001$. Friedman post hoc comparisons confirmed significant differences between every pair of frequency bands. The paired comparisons also showed large standardized effects, particularly for theta versus low-gamma (Cohen's $|d_z| = 2.68$), theta versus beta ($|d_z| = 1.96$), and alpha versus low-gamma ($|d_z| = 1.89$). Correlations between bands were generally positive, with the strongest associations observed between theta and low-gamma (r = 0.498), alpha and beta (r = 0.584), and beta and low-gamma (r = 0.581), whereas the theta–alpha relationship was weak (r = 0.090). Because the sign of Cohen's d depends on the order in which the bands were compared, the absolute effect-size values are reported here to emphasize the magnitude of the differences.

PCR3 showed a pronounced and progressive increase in activity across the frequency bands. Mean PCR3 values increased from 1.07 ± 0.76 in the theta band to 3.02 ± 1.97 in the alpha band, 7.17 ± 2.73 in the beta band, and 16.31 ± 4.40 in the low-gamma band. A repeated-measures ANOVA revealed a highly significant main effect of frequency band, $F(3, 291) = 1027.6$, $p < 0.001$. This effect remained significant after Greenhouse–Geisser correction ($p < 0.001$) and was associated with a very large effect size (partial eta squared approximately, $\eta = 0.91$, calculated from the reported sums of squares). Bonferroni-adjusted pairwise comparisons showed significant differences between all frequency bands, with PCR3 increasing progressively from theta to alpha, beta, and low-gamma (all adjusted $p < .001$). Consistent with the parametric analysis, the Friedman test demonstrated a significant overall effect of frequency band, $\chi2(3) = 284.93$, $p < 0.001$. Friedman post hoc comparisons confirmed significant differences between every pair of frequency bands. The paired comparisons also indicated large to very large standardized effects, particularly for theta versus low-gamma (Cohen's $|d_z| = 3.69$), alpha versus low-gamma ($|d_z| = 3.70$), and beta versus low-gamma ($|d_z| = 3.25$). Correlations between bands were generally positive, with the strongest association observed between the beta and low-gamma bands (r = 0.789), followed by the alpha–beta (r = 0.640) and alpha–low-gamma (r = 0.597) relationships. The theta-band PCR3 values showed weaker associations with the other bands, ranging from r = 0.265 for theta versus beta to r = 0.437 for theta versus low-gamma.

Across all three phase-cone rate measures, PCR activity varied significantly as a function of frequency band, but the pattern of variation differed among PCR1, PCR2, and PCR3. PCR1 showed relatively

modest frequency dependence: its mean value increased from the theta band (11.91) to the alpha band (18.74) and beta band (26.18), with a comparable value in the low-gamma band (26.88). In contrast, PCR2 exhibited a progressive increase across all bands, from 3.38 in theta to 23.13 in low-gamma, with the largest increase occurring between the beta and low-gamma bands. PCR3 showed the most pronounced frequency-dependent gradient, increasing from 1.07 in theta to 3.02 in alpha, 7.17 in beta, and 16.31 in low-gamma. Thus, PCR1 was relatively distributed across the beta and low-gamma bands, whereas PCR2 and particularly PCR3 were increasingly dominated by low-gamma activity. All three measures showed significant overall band effects, with the largest effect for PCR3, followed by PCR2 and PCR1.

The comparison between the μECoG signal and the phase-cone rates suggests that PCR measures may provide a more sensitive and temporally resolved characterization of seizure-related dynamics than broadband signal amplitude alone. Although the μECoG recording in Fig. 2A shows a broad increase in amplitude and variability during the latter portion of the seizure, the PCR measures reveal more subtle, intermittent, and frequency-specific changes that are not fully captured by the amplitude envelope. In particular, PCR1 exhibits distinct beta- and low-gamma-band fluctuations, whereas PCR2 and PCR3 show progressively stronger low-gamma dominance. These changes may reflect alterations in the organization and coordination of phase relationships that can occur without a proportional change in broadband ECoG amplitude. Thus, PCR1, PCR2, and PCR3 may serve as complementary biomarkers of ictal dynamics, potentially detecting fine-grained changes in seizure-related network organization that are less apparent in conventional amplitude-based measures.

4.2 PCR Activity during Reading Task

The temporal dynamics of the PCRs during the book-reading task are illustrated in Fig. 4. The raw interictal μECoG signal (Fig. 4A) exhibits continuous activity within the 3–50 Hz range at electrode #28. When decomposed into specific frequency bands, the PCR counts (Fig. 4B–E) demonstrate a clear spectral gradient; the magnitude of PCR occurrences increases progressively from the theta band through the alpha and beta bands, reaching its peak in the low-gamma band. This visual trend is consistent with the repeated-measures ANOVA results, which confirmed a significant main effect of the frequency band ($p < 0.001$).

Across the different frequency bands, a distinct hierarchy is observed among the PCR categories. PCR1 (blue) and PCR2 (black) consistently maintain higher counts compared to PCR3 (red), particularly in the higher frequency beta and low-gamma bands. Figure 5 provides a high-resolution temporal view of a 20-second window (45–65 s) extracted from Fig. 4. This magnified view reveals the fine-grained fluctuations of the PCR counts and highlights the temporal alignment of peaks across the different spectral bands, suggesting a coordinated modulation of phase coherence across frequencies during the reading task.

Descriptive analysis of the PCR1 data revealed a progressive increase in magnitude across the four frequency bands, with the lowest values observed in the theta band (mean ± SD = 0.36 ± 0.20) and the

highest in the low-gamma band (mean ± SD = 16.89 ± 1.54). Pearson correlation analysis indicated that the frequency bands were largely independent, with all correlation coefficients remaining weak ($r < 0.22$), the strongest relationship being observed between the alpha and beta bands ($r = 0.22$).

To evaluate the differences between the frequency bands, a repeated-measures ANOVA was conducted. The analysis revealed a highly significant main effect of the frequency band, $F(3, 294) = 6300$, $p < .001$. Bonferroni-corrected post hoc comparisons confirmed that all pairwise differences were statistically significant (all adjusted $p < .001$), with the magnitudes following the order: low-gamma > beta > alpha > theta. These results were further validated using the non-parametric Friedman test, which similarly demonstrated significant differences across the bands ($\chi2(3) = 295.8$, $p < .001$), with all post hoc comparisons reaching significance ($p < .001$). The magnitude of these differences was substantial, as evidenced by paired Cohen's d_z effect sizes, which ranged from large to very large, peaking at the comparison between theta and low-gamma ($|dz| = 10.63$).

PCR1 showed a clear frequency-dependent increase across bands, with mean ± SD values of 0.36 ± 0.20 in theta, 1.44 ± 0.67 in alpha, 4.67 ± 0.90 in beta, and 16.89 ± 1.54 in low-gamma. A repeated-measures ANOVA demonstrated a strong main effect of band on PCR1 ($F(3, 294) = 6300$, $p < .001$), which was corroborated by a Friedman test ($\chi^2(3) = 296$, $p < .001$). Post hoc Bonferroni-corrected pairwise comparisons indicated that all band pairs differed significantly (all adjusted $p < .001$), with very large paired effect sizes (Cohen's $|d_z| = 1.55–10.63$), confirming the ordering low-gamma > beta > alpha > theta. Pairwise correlations between bands were generally weak, indicating that the band-specific PCR1 values were largely distinct.

PCR2 also showed a strong frequency-dependent increase across bands, with mean ± SD values of 0.19 ± 0.14 in theta, 0.68 ± 0.28 in alpha, 2.67 ± 0.44 in beta, and 10.52 ± 1.16 in low-gamma. A repeated-measures ANOVA revealed a robust main effect of band on PCR2 ($F(3, 294) = 5480$, $p < .001$), which was confirmed by a Friedman test ($\chi^2(3) = 295$, $p < .001$). Bonferroni-corrected post hoc comparisons showed that all band pairs differed significantly (all adjusted $p < .001$), with the largest values in low-gamma, followed by beta, alpha, and theta. The paired Cohen's d_z values indicated very large effects across all comparisons ($|d_z| = 1.63–8.83$), supporting a strong separation between bands. Pairwise correlations were weak, indicating that PCR2 values were largely distinct across frequency bands.

PCR3 showed a strong frequency-dependent increase across bands, with mean ± SD values of 0.15 ± 0.10 in theta, 0.60 ± 0.27 in alpha, 2.27 ± 0.42 in beta, and 9.02 ± 0.99 in low-gamma. A repeated-measures ANOVA demonstrated a robust main effect of band on PCR3 ($F(3, 294) = 5342$, $p < 0.001$), which was confirmed by a Friedman test ($\chi^2(3) = 291$, $p < .001$). Bonferroni-corrected post hoc comparisons indicated that all band pairs differed significantly (all adjusted $p < .001$), with the expected ordering low-gamma > beta > alpha > theta. The paired Cohen's dz values were very large across all comparisons ($|d_z| = 1.54–8.89$), indicating strong effect sizes and clear separation among frequency bands.

4.3 Compare Seizure and Reading

The temporal dynamics of PCRs during the interictal book-reading task are illustrated in Fig. 4. The raw μECoG signal (Fig. 4A) remained relatively stable in amplitude throughout the task. When decomposed into specific frequency bands, the PCR counts (Fig. 4B–E) demonstrated a clear spectral gradient, where the magnitude of PCRs increased progressively from the theta band through the alpha and beta bands, reaching a peak in the low-gamma band. This visual trend is consistent with our statistical analysis, which confirmed a significant main effect of the frequency band ($F(3, 294) = 6300$, $p < 0.001$). A magnified temporal view (Fig. 5) reveals that the reading task is characterized by low-amplitude, steady-state fluctuations, with PCR1 (derived from y(t)) and PCR2 (derived from y'(t)) consistently maintaining higher rates than PCR3 (derived from y"(t)).

In contrast, the ictal seizure activity (Figs. 2 and 3) revealed a profound amplification of PCRs. The raw ictal μECoG signal exhibited a characteristic crescendo, with a massive increase in voltage and oscillation power over time (Fig. 2A). This was mirrored in the PCR dynamics; while the spectral hierarchy (low-gamma> beta > alpha > theta) was preserved, the absolute magnitude of the rates increased drastically. Specifically, the PCR counts in the low-gamma band, which peaked at approximately 20 during reading, reached magnitudes of up to 60 during the ictal event (Fig. 2E).

A comparative analysis of the temporal dynamics further distinguishes the two states. While reading produced consistent, low-level oscillations (Fig. 5), the seizure period was characterized by high-amplitude, erratic bursts of PCRs (Fig. 3). Throughout both states, PCR1 remained the dominant biomarker, but the spiking behavior of both PCR1 and PCR2 was significantly more pronounced during the seizure. This suggests that the transition to an ictal state is marked not only by an increase in the volume of phase-cone activity but by an intensification of the velocity and acceleration of phase transitions.

5. Discussion

The present study demonstrates that stable phase-cone formations can be reliably detected in human micro-electrocorticographic (μECoG) recordings not only from the original cortical signal but also from its first and second temporal derivatives. Across all three measures, phase-cone rates (PCRs) exhibited a highly consistent spectral hierarchy, increasing progressively from theta to low-gamma frequencies during both seizure and reading conditions. Furthermore, seizure activity produced substantially higher PCR magnitudes and greater temporal variability than cognitively engaged but interictal cortical activity. Together, these findings support the hypothesis that mesoscopic cortical state transitions can be quantified through phase-cone dynamics and suggest that derivative-based phase-cone measures provide complementary information regarding the temporal evolution of cortical reorganization (Freeman 2000, 2004, 2005; Kozma and Freeman 2016).

5.1 Phase-cone dynamics and cortical state transitions

One of the most striking observations was the monotonic increase in phase-cone rates from theta through low-gamma frequencies. This spectral hierarchy was preserved across PCR1, PCR2, and PCR3 and remained robust during both cognitive and epileptic states. This consistency suggests that phase-cone formation reflects a fundamental property of cortical organization rather than a task-specific phenomenon.

Higher-frequency oscillations are generally associated with local cortical computations, rapid synaptic interactions, and transient neuronal assemblies (Buzsáki and Draguhn 2004; Fries 2005). Because these oscillations operate over shorter temporal scales, they can support more frequent reorganizations of cortical activity, thereby increasing the probability of detecting stable phase-cone structures. In contrast, slower rhythms such as theta oscillations are associated with longer integration windows and broader spatial coordination (von Stein and Sarnthein 2000; Buzsáki 2006), naturally resulting in fewer detectable phase-transition events per unit time.

The preservation of this frequency hierarchy across all signal transformations suggests that the generation of phase cones reflects a scale-independent property of cortical dynamics. Similar multiscale organization has been reported for cortical traveling waves, phase discontinuities, and spatial amplitude patterns across diverse electrophysiological recordings (Freeman and Rogers 2002; Freeman et al. 2003). The present findings therefore support the view that phase-cone formation is a fundamental manifestation of ongoing cortical self-organization.

5.2 Physiological interpretation of PCR1, PCR2, and PCR3

A major contribution of this study is the demonstration that organized phase-cone activity persists after temporal differentiation of the cortical signal. Although phase cones have traditionally been studied using the original electrophysiological signal, little attention has been directed toward understanding how these structures behave in higher-order temporal representations.

PCR1 quantifies phase-cone formation in the original μECoG signal and therefore reflects the occurrence of mesoscopic state transitions in cortical activity. PCR2, derived from the first temporal derivative, emphasizes the velocity of ongoing cortical reconfigurations and may be viewed as a measure of how rapidly phase relationships evolve across neuronal populations. PCR3, derived from the second temporal derivative, highlights acceleration-like changes and may therefore capture abrupt transitions, transient instabilities, or rapid recruitment events that are less apparent in lower-order measures.

Importantly, differentiation suppresses slow background fluctuations while accentuating rapid transient dynamics. The observation that stable phase cones remained detectable following first- and second-order differentiation suggests that cortical state transitions are encoded not only in instantaneous phase patterns but also in the rates at which these patterns evolve. Thus, PCR2 and PCR3 appear to provide information that complements traditional analyses of oscillatory power, synchronization, and phase locking (Le Van Quyen et al. 2001; Breakspear 2004).

The lower overall counts observed for PCR3 relative to PCR1 and PCR2 are physiologically plausible. Acceleration-based events would be expected to represent a more selective subset of cortical transitions, corresponding to episodes of particularly rapid network reorganization. Consequently, the three PCR measures may be viewed as complementary descriptors of cortical dynamics at progressively higher temporal orders.

5.3 Seizure-related amplification of phase-transition dynamics

The seizure recordings exhibited marked increases in both PCR magnitude and temporal variability relative to the reading condition. Particularly notable were intermittent bursts of beta- and low-gamma-band activity that were absent or greatly attenuated during normal cognitive processing.

Traditionally, epilepsy has been described as a disorder of excessive synchronization. More recent work, however, indicates that seizure evolution involves complex interactions among synchronization, desynchronization, fragmentation, and large-scale network recruitment (Le Van Quyen et al. 2003; Schiff et al. 2005). From this perspective, elevated PCR activity may reflect intensified phase-transition dynamics associated with repeated epileptic network reorganization during seizure evolution. The substantial variability observed during seizures further supports this interpretation. In contrast to the relatively stable and constrained PCR fluctuations observed during reading, ictal activity generated transient surges that likely reflect episodes of rapid network destabilization and recruitment. Similar dynamical fluctuations have been reported in studies of seizure propagation, cortical traveling waves, and mesoscale synchronization patterns (Smith et al. 2016; Martinet et al. 2017).

These observations suggest that phase-cone measures quantify aspects of seizure dynamics that are not fully captured by conventional amplitude-based analyses. Because PCR metrics directly measure spatiotemporal phase-transition events, they may provide a complementary biomarker for characterizing seizure initiation, propagation, and termination.

5.4 Relationship to Freeman's neurodynamics framework

The present findings are highly consistent with Freeman's theory of cortical neurodynamics, which proposes that cognition emerges through rapid transitions among metastable cortical states rather than through static patterns of neural activity (Freeman 2000, 2004, 2005). According to this framework, cortical populations continually self-organize into transient assemblies that form, dissolve, and reform on time scales of tens to hundreds of milliseconds.

Freeman and colleagues proposed that phase discontinuities and phase cones represent mesoscopic markers of these state transitions (Freeman and Barrie 2000; Freeman et al. 2003). Within this interpretation, the stable phase cones detected during reading may reflect normal cortical processing involving continual transitions among transient cognitive states. The relatively stable PCR fluctuations observed during reading are consistent with the notion of healthy cortical metastability, in which state transitions occur continuously but remain constrained within functional limits.

In contrast, seizure activity appears to represent a pathological alteration of this metastable regime. Rather than exhibiting balanced transitions among transient cortical states, the epileptic cortex showed periods of excessive and highly variable phase-transition activity. The resulting amplification of PCR measures may reflect abnormal departures from the dynamic equilibrium that characterizes healthy cortical function.

A particularly important implication of the present findings is that state-transition dynamics remain observable in the first and second temporal derivatives of the signal. This observation suggests that not only cortical states themselves, but also the velocity and acceleration of cortical reorganization, carry meaningful physiological information. In this sense, PCR2 and PCR3 extend Freeman's original framework by providing quantitative measures of higher-order dynamical processes that accompany metastable state transitions.

5.5 Implications for cognitive neurodynamics

The concept of metastability has become increasingly important in contemporary theories of brain function (Kelso 1995; Varela et al. 2001; Kozma and Freeman 2016). These theories emphasize that cognition arises from continual transitions among partially synchronized neuronal populations rather than from static patterns of activation. The present results support this perspective by demonstrating persistent phase-cone activity during both normal cognition and pathological seizure activity. The findings suggest that PCR measures may provide a useful experimental tool for quantifying metastable cortical dynamics across multiple temporal scales.

Because the derivative-based measures remained physiologically meaningful, future investigations may benefit from examining whether PCR2 and PCR3 reveal subtle dynamical changes that precede overt alterations in oscillatory power, synchronization, or behavioral performance. Such measures may prove particularly valuable in studies of epilepsy, aging, neurodegenerative disease, disorders of consciousness, and cognitive decline where alterations in network dynamics may precede structural pathology.

5.6 Limitations and future directions

Several limitations should be acknowledged. First, the study analyzed recordings from a single seizure from one cortical region in one participant, limiting the generalizability of the findings. Replication across larger patient cohorts and multiple seizure types is necessary to assess the robustness of the observed effects.

Second, recordings were obtained from a localized microgrid positioned near a seizure onset zone and therefore may not fully capture dynamics occurring in more distributed cortical networks. Third, although surrogate analyses strongly support the physiological validity of the detected phase cones, additional validation using independent datasets and alternative analytical approaches would further strengthen confidence in these findings.

Future studies should investigate phase-cone dynamics across a wider range of cognitive tasks, behavioral states, and neurological disorders. Simultaneous analyses of PCR measures, spectral power, synchronization indices, phase-amplitude coupling, neuronal avalanches, and traveling cortical waves may provide deeper insight into the mechanisms underlying cortical state transitions (Beggs and Plenz 2003; Varela et al. 2001). Longitudinal investigations could also determine whether derivative-based PCR measures possess predictive value for seizure forecasting or treatment monitoring.

5.7 Conclusions

Stable phase-cone dynamics were reliably detected in human μECoG recordings and remained observable after first- and second-order temporal differentiation of the signal. Phase-cone rates exhibited a robust spectral hierarchy that increased progressively from theta to low-gamma frequencies and showed substantially greater magnitude and variability during seizure activity than during reading. These findings indicate that phase-transition dynamics are preserved across multiple dynamical representations of cortical activity and support the view that phase-cone measures capture fundamental aspects of mesoscopic brain organization. Derivative-based PCR metrics provide novel information regarding the velocity and acceleration of cortical state transitions and may offer a useful framework for investigating normal cognition, epileptic dynamics, and other conditions involving large-scale cortical reorganization.

This study is offered in recognition of the centennial of Walter J. Freeman and in memory of Mark D. Holmes, whose collaborative contributions helped advance the study of cortical dynamics and epilepsy.

Abbreviations

μECoG:	micro-electrocorticography
PCR	Phase-cone rate
PCRs	Phase-cone rates
PCR1	PCR extracted from y(t) = μECoG
PCR2	PCR extracted from the first derivative of y(t); y'(t) = dy/dt
PCR3	PCR extracted from the second derivative of y(t); y"(t) = dy'/dt

Declarations

6. CRediT authorship contribution statement

Ceon Ramon: Conceptualization, Methodology, Software, Validation, Formal analysis, Writing – original draft, Visualization. **Alexander Doud**: Data curation, Software development, Validation, Writing – review and editing. **Shahin Hakimian**: Conceptualization, Methodology, Writing – review and editing. **Nicholas P.**

Poolos: Writing – review and editing, Supervision, Project administration, Funding and resources acquisition.

7. Conflict of Interests

All authors declare that there is no conflict of interest. The authors declare that no funds, grants, or other support were received during the preparation of this manuscript.

8. Data Availability

The microgrid μECoG dataset analyzed in this study is publicly available through the Open Science Framework (OSF) repository at https://osf.io/gyqah/. It is operated by the Center for Open Science. Also, the same data is available from the corresponding author, Ceon Ramon.

9. Funding Declaration

The authors declare that they received no funds, grants, or other support during the preparation of this manuscript.

Declaration of Generative AI and AI-assisted technologies in the writing process

MATLAB Copilot was used to assist in the development, debugging, and refinement of analysis software. It was also used for limited language editing during manuscript preparation. All code, analyses, interpretations, and manuscript text were independently reviewed and verified by the authors, who assume full responsibility for the final published content.

References

1. Beggs JM, Plenz D (2003) Neuronal avalanches in neocortical circuits. J Neurosci 23(35):11167–11177. https://doi.org/10.1523/JNEUROSCI.23-35-11167.2003
2. Bhattacharya BS, Coyle D, Maguire LP (2011) A thalamo-cortico-thalamic neural mass model to study alpha rhythms in Alzheimer's disease. Neural Netw 24(6):631–645. https://doi.org/10.1016/j.neunet.2011.02.009
3. Breakspear M (2004) Dynamic connectivity in neural systems: theoretical and empirical considerations. Neuroinformatics 2(2):205–226. https://doi.org/10.1385/NI:2:2:205
4. Brydges CR (2019) Effect size guidelines, sample size calculations, and statistical power in gerontology. Innov Aging 3(4):igz036. https://doi.org/10.1093/geroni/igz036
5. Buzsáki G, Draguhn A (2004) Neuronal oscillations in cortical networks. Science 304(5679):1926–1929. https://doi.org/10.1126/science.1099745
6. Cohen J (1992) A power primer. Psychol Bull 112(1):155–159. https://doi.org/10.1037//0033-2909.112.1.155

7. Freeman WJ (1975) Mass Action in the Nervous System: Examination of the Neurophysiological Basis of Adaptive Behavior Through the EEG. Academic Press, New York. 489 pp. ISBN 978-0-12-267150-0
8. Freeman WJ (2000) Neurodynamics: An Exploration in Mesoscopic Brain Dynamics. Springer, London. ISBN 9781852336165
9. Freeman WJ (2005) A field-theoretic approach to understanding scale-free neocortical dynamics. Biol Cybern 92:350–359. https://doi.org/10.1007/s00422-005-0563-1
10. Freeman WJ, Barrie JM (2000) Analysis of spatial patterns of phase in neocortical gamma EEGs in rabbit. J Neurophysiol 84(3):1266–1278. https://doi.org/10.1152/jn.2000.84.3.1266
11. Freeman WJ, Burke BC, Holmes MD (2003) Aperiodic phase re-setting in scalp EEG of beta-gamma oscillations by state transitions at alpha-theta rates. Hum Brain Mapp 19(4):248–272. https://doi.org/10.1002/hbm.10120
12. Freeman WJ, Holmes MD, Burke BC, Vanhatalo S (2003) Spatial spectra of scalp EEG and EMG from awake humans. Clin Neurophysiol 114(6):1053–1068. https://doi.org/10.1016/s1388-2457(03)00045-2
13. Freeman WJ (2004) Origin, structure, and role of background EEG activity. Part 2. Analytic phase. Clin Neurophysiol 115:2089–2107. https://doi.org/10.1016/j.clinph.2004.02.028
14. Freeman WJ, Holmes MD (2005) Metastability, instability, and state transitions in neocortex. Neural Netw 18(5–6):497–504. https://doi.org/10.1016/j.neunet.2005.06.014
15. Freeman WJ, Holmes MD, West GA, Vanhatalo S (2006a) Dynamics of human neocortex that optimizes its stability and flexibility. Int J Intell Syst 21(9):881–901. https://doi.org/10.1002/int.20167
16. Freeman WJ, Holmes MD, West GA, Vanhatalo S (2006b) Fine spatiotemporal structure of phase in human intracranial EEG. Clin Neurophysiol 117(6):1228–1243. https://doi.org/10.1016/j.clinph.2006.03.012
17. Freeman WJ, Vitiello G (2006) Nonlinear brain dynamics as macroscopic manifestation of underlying many-body dynamics. Phys Life Rev 3(2):93–118. https://doi.org/10.1016/j.plrev.2006.02.001
18. Freeman WJ, Kozma R (2010) Freeman's mass action. Scholarpedia 5(1):8040. https://doi.org/10.4249/scholarpedia.8040
19. Freeman WJ, Quiroga RQ (2013) Basic concepts for spatial analysis. Imaging brain function with EEG. Springer, New York, NY, pp 87–123. https://doi.org/10.1007/978-1-4614-4984-3_6
20. Fries P (2005) A mechanism for cognitive dynamics: neuronal communication through neuronal coherence. Trends Cogn Sci 9(10):474–480. https://doi.org/10.1016/j.tics.2005.08.011
21. Innocenti GM, Vercelli A, Caminiti R (2014) The diameter of cortical axons depends both on the area of origin and target. Cereb Cortex 24(8):2178–2188. https://doi.org/10.1093/cercor/bht070

22. Jansen BH, Rit VG (1995) Electroencephalogram and visual evoked potential generation in a mathematical model of coupled cortical columns. Biol Cybern 73(4):357–366. https://doi.org/10.1007/BF00199471
23. Jirsa V, Wang H, Triebkorn P, Hashemi M, Jha J, Gonzalez-Martinez J, Guye M, Makhalova J, Bartolomei F (2023) Personalised virtual brain models in epilepsy. Lancet Neurol 22(5):443–454. https://doi.org/10.1016/S1474-4422(23)00008-X
24. Kozma R, Puljic M, Balister P, Bollobás B, Freeman WJ (2005) Phase transitions in the neuropercolation model of neural populations with mixed local and non-local interactions. Biol Cybern 92(6):367–379. https://doi.org/10.1007/s00422-005-0565-z
25. Kozma R, Freeman WJ (2008) Intermittent spatio-temporal desynchronization and sequenced synchrony in ECoG signals. Chaos 18(3):037131. https://doi.org/10.1063/1.2979694
26. Kozma R (2016) Reflections on a giant of brain science: How lucky we are having Walter J. Freeman as our beacon in cognitive neurodynamics research. Cogn Neurodyn 10(6):457–469. https://doi.org/10.1007/s11571-016-9403-3
27. Kozma R, Freeman WJ (2016) Cognitive phase transitions in the cerebral cortex: enhancing the neuron doctrine by modeling neural fields. Stud Syst Decis Control 39. Springer, Cham. https://doi.org/10.1007/978-3-319-24406-8
28. Kozma R, Freeman WJ (2017) Cinematic operation of the cerebral cortex interpreted via critical transitions in self-organized dynamic systems. Front Syst Neurosci 11:10. https://doi.org/10.3389/fnsys.2017.00010
29. Lancaster G, Iatsenko D, Pidde A, Ticcinelli V, Stefanovska A (2018) Surrogate data for hypothesis testing of physical systems. Phys Rep 748:1–60. https://doi.org/10.1016/j.physrep.2018.06.001
30. e Van Quyen M, Foucher J, Lachaux JP, Rodriguez E, Lutz A, Martinerie J, Varela FJ (2001) Comparison of Hilbert transform and wavelet methods for the analysis of neuronal synchrony. J Neurosci Methods 111(2):83–98. https://doi.org/10.1016/S0165-0270(01)00372-7
31. e Van Quyen M, Navarro V, Martinerie J, Baulac M, Varela FJ (2003) Toward a neurodynamical understanding of ictogenesis. Epilepsia 44(Suppl 12):30–43. https://doi.org/10.1111/j.0013-9580.2003.12007.x
32. Martinet LE, Fiddyment G, Madsen JR, Eskandar EN, Truccolo W, Eden UT, Cash SS, Kramer MA (2017) Human seizures couple across spatial scales through travelling wave dynamics. Nat Commun 8:14896. https://doi.org/10.1038/ncomms14896
33. Moran R, Pinotsis DA, Friston KJ (2013) Neural masses and fields in dynamic causal modeling. Front Comput Neurosci 7:57. https://doi.org/10.3389/fncom.2013.00057
34. Myers MH, Kozma R, Davis JJ, Ilin R (2014) Phase cone detection optimization in EEG data. In: Proceedings of the 2014 International Joint Conference on Neural Networks (IJCNN). IEEE, Piscataway, NJ, pp 2504–2511. https://doi.org/10.1109/IJCNN.2014.6889880
35. Panagiotides H, Freeman WJ, Holmes MD, Pantazis D (2011) Behavioral states may be associated with distinct spatial patterns in electrocorticogram. Cogn Neurodyn 5(1):55–66.

https://doi.org/10.1007/s11571-010-9139-4

36. Pinotsis DA, Moran RJ, Friston KJ (2012) Dynamic causal modeling with neural fields. NeuroImage 59(2):1261–1274. https://doi.org/10.1016/j.neuroimage.2011.08.020
37. Ramon C, Holmes MD, Freeman WJ, McElroy R, Rezvanian E (2008) Comparative analysis of temporal dynamics of EEG and phase synchronization of EEG to localize epileptic sites from high density scalp EEG interictal recordings. Annual International Conference of the IEEE Engineering in Medicine and Biology Society. IEEE Engineering in Medicine and Biology Society. Annual International Conference, 2008, 4548–4550. https://doi.org/10.1109/IEMBS.2008.4650224
38. Ramon C, Freeman WJ, Holmes M, Ishimaru A, Haueisen J, Schimpf PH, Rezvanian E (2009) Similarities between simulated spatial spectra of scalp EEG, MEG and structural MRI. Brain Topogr 22(3):191–196. https://doi.org/10.1007/s10548-009-0104-7
39. Ramon C, Holmes MD, Freeman WJ (2013) Increased phase clustering in epileptogenic areas measured with 256-channel dense array EEG. J Neurol Transl Neurosci 2:1029. https://www.jscimedcentral.com/public/assets/articles/neuroscience-2-1029.pdf
40. Ramon C, Holmes MD, Wise MV, Tucker D, Jenson K, Kinn SR (2018) Oscillatory patterns of phase cone formations near to epileptic spikes derived from 256-channel scalp EEG data. Comput Math Methods Med 2018:9034543. https://doi.org/10.1155/2018/9034543
41. Ramon C, Holmes MD (2020) Increased phase cone turnover in 80–250 Hz bands occurs in the epileptogenic zone during interictal periods. Front Hum Neurosci 14:615744. https://doi.org/10.3389/fnhum.2020.615744
42. Ramon C, Graichen U, Gargiulo P, Zanow F, Knösche TR, Haueisen J (2023) Spatiotemporal phase slip patterns for visual evoked potentials, covert object naming tasks, and insight moments extracted from 256 channel EEG recordings. Front Integr Neurosci 17:1087976. https://doi.org/10.3389/fnint.2023.1087976
43. Ramon C, Doud A, Holmes MD (2024) Decrease in phase slip rates and phase cone structures during seizure evolution and epileptogenic activities derived from microgrid ECoG data. Curr Res Neurobiol 6:100126. https://doi.org/10.1016/j.crneur.2024.100126
44. Ramon C, Gargiulo P (2025) Phase slips extracted from derivatives of EEG data provide a deeper insight into the formation of cortical phase transitions. Front Integr Neurosci 19:1471120. https://doi.org/10.3389/fnint.2025.1471120
45. Richardson JT (2011) Eta squared and partial eta squared as measures of effect size in educational research. Educ Res Rev 6:135–147. https://doi.org/10.1016/j.edurev.2010.12.001
46. Ruiz Y, Li G, González E, Freeman WJ (2008) A New Approach to Detect Stable Phase Structure in High-Density EEG Signals. In: Wang R, Shen E, Gu F (eds) Advances in Cognitive Neurodynamics—ICCN 2007. Springer, Dordrecht, pp 741–745. https://doi.org/10.1007/978-1-4020-8387-7_128
47. Ruiz Y, Pockett S, Freeman WJ, Gonzalez E, Li G (2010) A method to study global spatial patterns related to sensory perception in scalp EEG. J Neurosci Methods 191:110–118. https://doi.org/10.1016/j.jneumeth.2010.05.021

48. Swadlow HA, Waxman SG (2012) Axonal conduction delays. Scholarpedia 7:1451. https://doi.org/10.4249/scholarpedia.1451
49. Schiff SJ, Sauer T, Kumar R, Weinstein SL (2005) Neuronal spatiotemporal pattern discrimination: The dynamical evolution of seizures. NeuroImage 28(4):1043–1055. https://doi.org/10.1016/j.neuroimage.2005.06.059
50. Smith EH, Liou JY, Davis TS, Merricks EM, Kellis SS, Weiss SA, Greger B, House PA, McKhann GM RR II, Emerson RG, Bateman LM, Trevelyan AJ, Schevon CA (2016) The ictal wavefront is the spatiotemporal source of discharges during spontaneous human seizures. Nat Commun 7:11098. https://doi.org/10.1038/ncomms11098
51. Thatcher RW, North DM, Biver CJ (2009) Self-organized criticality and the development of EEG phase reset. Hum Brain Mapp 30(2):553–574. https://doi.org/10.1002/hbm.20524
52. Thatcher RW, North DM, Biver CJ (2014) LORETA EEG phase reset of the default mode network. Front Hum Neurosci 8:529. https://doi.org/10.3389/fnhum.2014.00529
53. Vaidyanathan PP (1993) Multirate Systems: Signals, Measurements, Implementation. Prentice-Hall, pp 80–110
54. Varela F, Lachaux JP, Rodriguez E, Martinerie J (2001) The brainweb: phase synchronization and large-scale integration. Nat Rev Neurosci 2(4):229–239. https://doi.org/10.1038/35067550
55. von Stein A, Sarnthein J (2000) Different frequencies for different scales of cortical integration: from local gamma to long-range alpha/theta synchronization. Int J Psychophysiol 38(3):301–313. https://doi.org/10.1016/s0167-8760(00)00172-0
56. Wang SH, Siebenhühner F, Arnulfo G, Myrov V, Nobili L, Breakspear M, Palva S, Palva JM (2023) Critical-like brain dynamics in a continuum from second- to first-order phase transition. J NeuroSci 43(45):7642–7656. https://doi.org/10.1523/JNEUROSCI.1889-22.2023
57. Wendling F, Bartolomei F, Bellanger J-J, Chauvel P (2002) Epileptic fast activity can be explained by a model of impaired GABAergic dendritic inhibition. Eur J Neurosci 15:1499–1508. https://doi.org/10.1046/j.1460-9568.2002.01985.x
58. Wendling F, Hernandez A, Bellanger J-J, Chauvel P, Bartolomei F (2005) Interictal to ictal transition in human temporal lobe epilepsy: insights from a computational model of intracerebral EEG. J Clin Neurophysiol 22:343–356. https://doi.org/10.1097/01.wnp.0000171397.02700.86

Figures

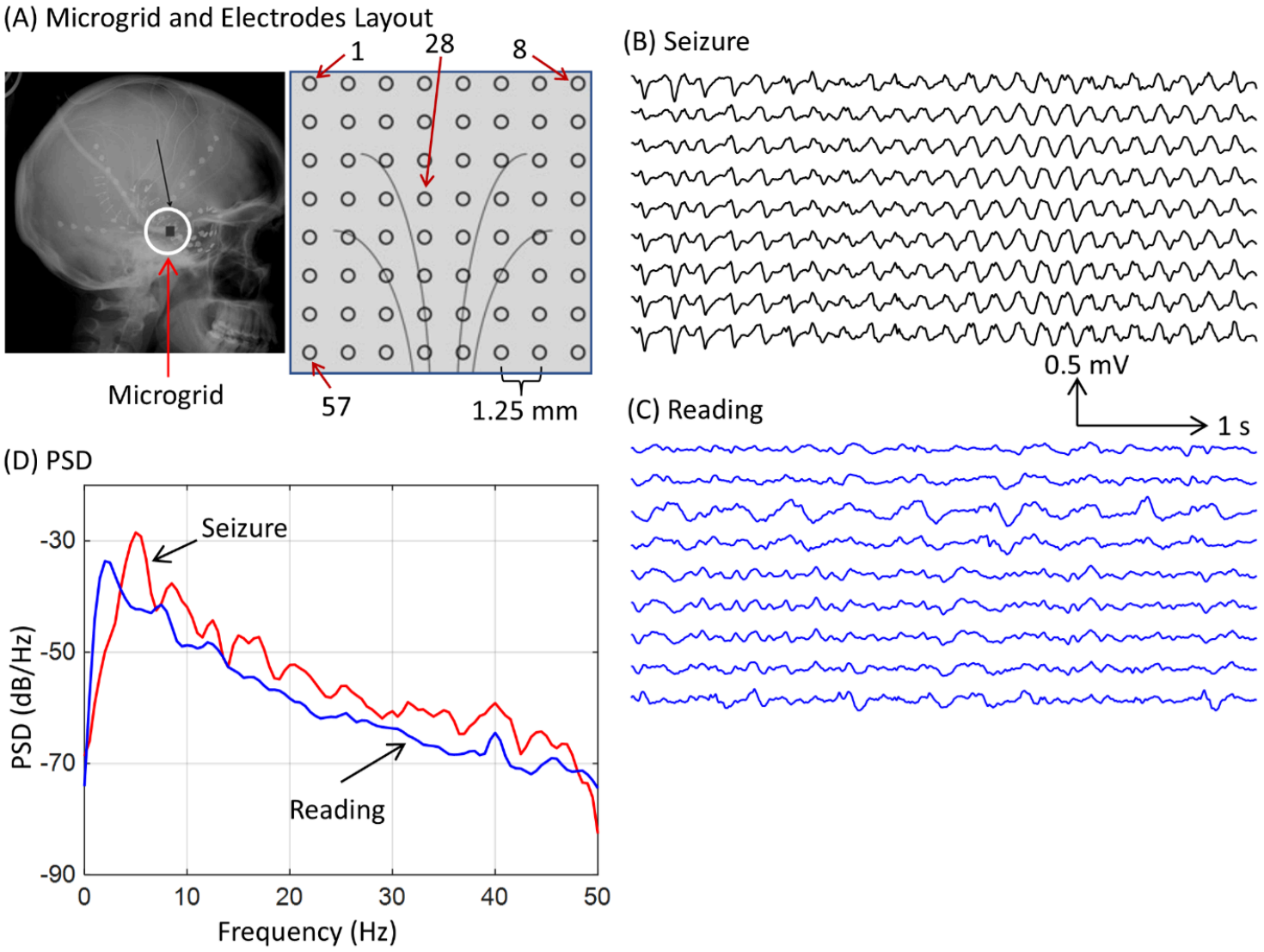


Figure 1

Representative μECoG traces and corresponding spectral profiles across distinct behavioral states. (A) X-ray of the skull showing the location of the 8 × 8 microgrid (white circle) and the layout of the microgrid electrodes. (B) A 5-second continuous segment of ictal data recorded during a generalized seizure event, illustrating highly synchronized, high-amplitude rhythmic waveforms. (C) Data captured during a normal cognitive reading task, demonstrating low-amplitude, desynchronized background cortical activity. Both time-series plots display eight channels extracted from the fourth row of an 8 × 8 microgrid array. (D) Grouped power spectral density (PSD) profiles combined across all eight channels, highlighting the quantitative shift from low-frequency dominance (delta and theta bands) during the ictal state to high-frequency activation (beta and low-gamma bands) during active text comprehension.

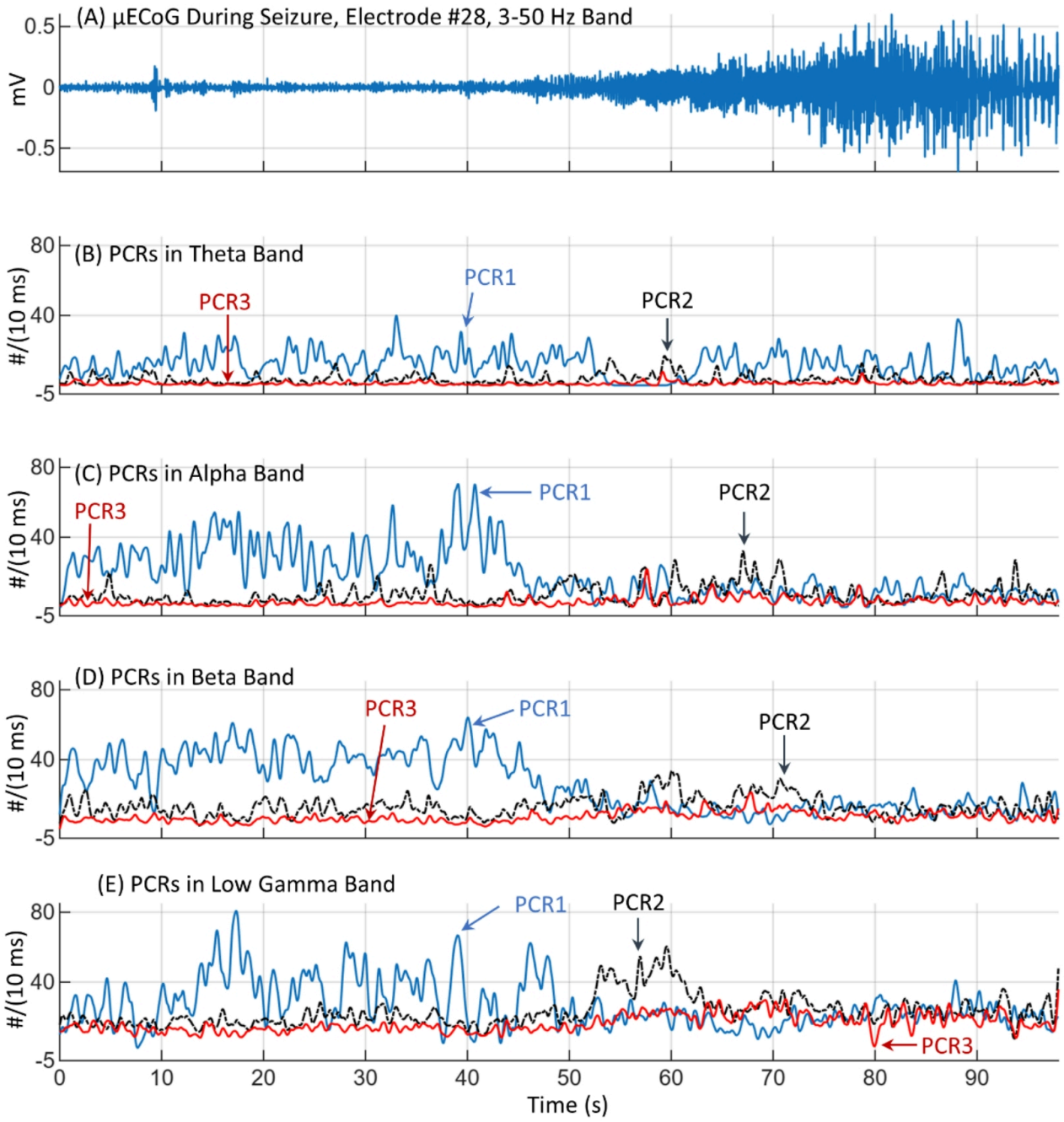


Figure 2

Ictal µECoG activity recorded from electrode #28 and the corresponding phase-cone rates (PCR1, PCR2, and PCR3) computed from y(t), y'(t), and y"(t), respectively, across frequency bands. (A) The 3–50 Hz band-limited µECoG signal over an approximately 100-s epoch, showing increased amplitude and variability during the latter portion of the recording. (B–E) PCR dynamics in the theta (3–7 Hz), alpha (7–12 Hz), beta (12–30 Hz), and low-gamma (30–50 Hz) bands, respectively. PCR1, PCR2, and PCR3 are shown in blue, black, and red, respectively.

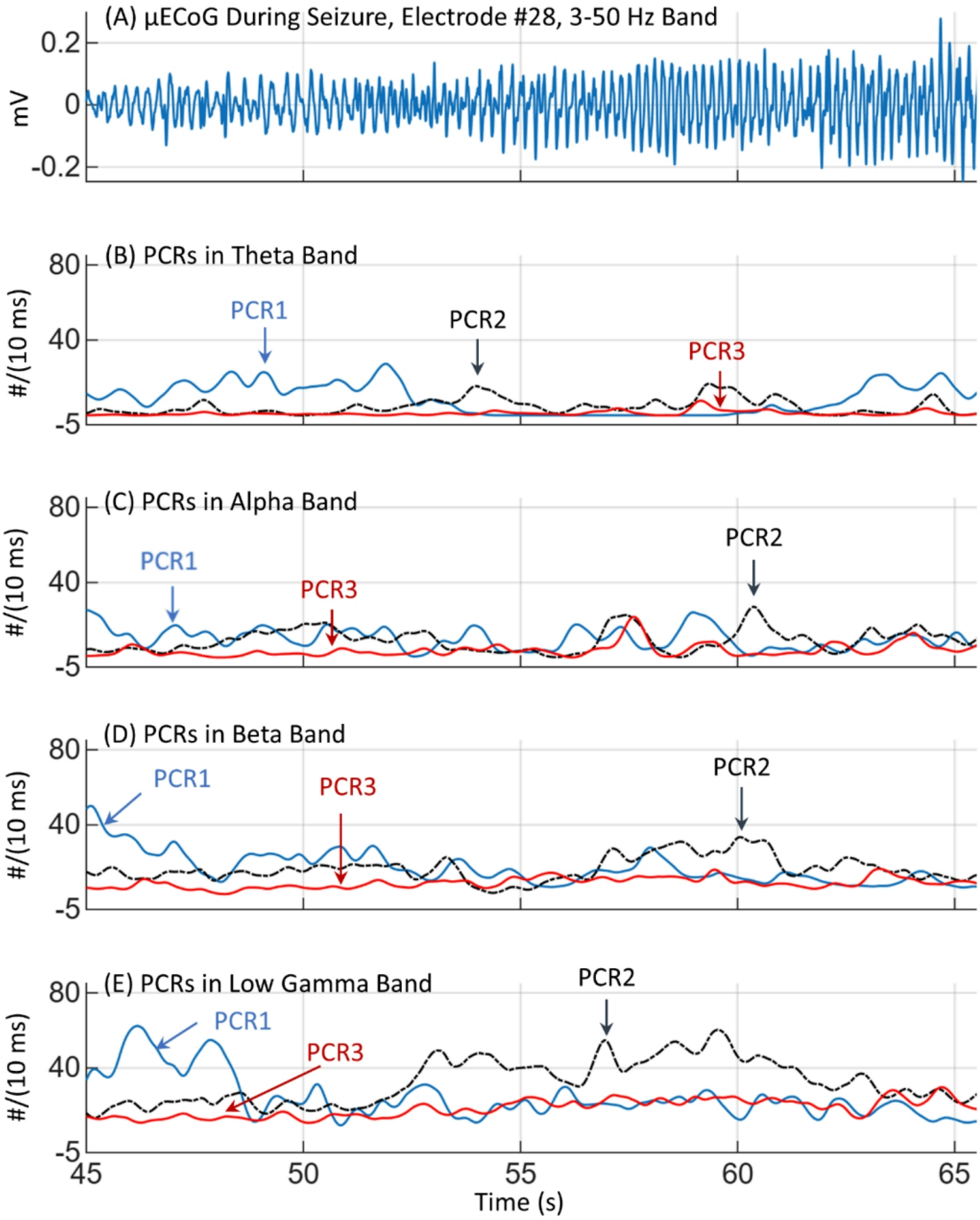


Figure 3

Detailed frequency-specific phase-cone dynamics during the 45–65 s ictal interval. Notice the suppression of theta-band PCR1 during this period.

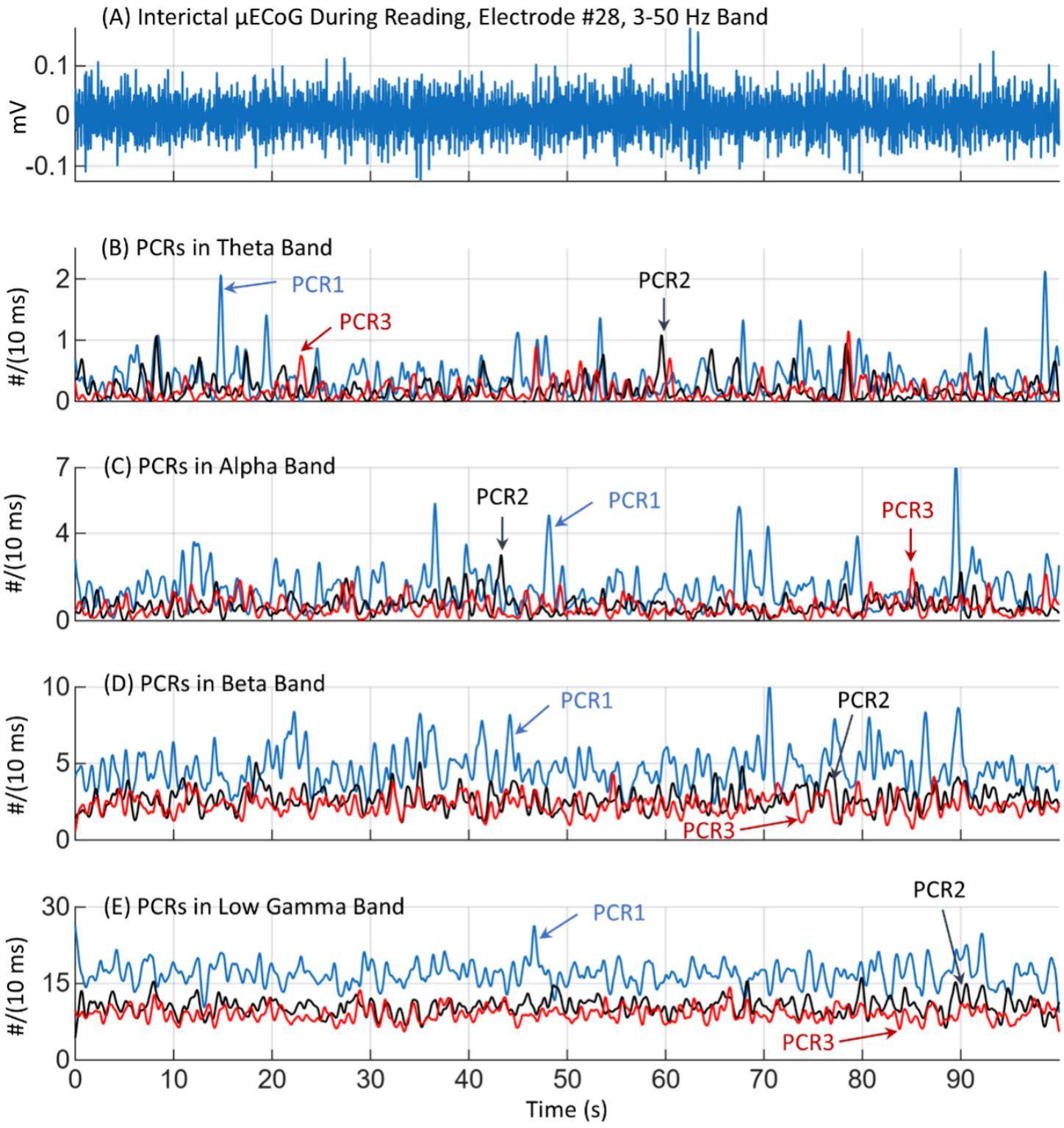


Figure 4

Spectral distribution of PCR counts during interictal book reading. (A) Representative raw µECoG signal (3–50 Hz) recorded from electrode #28. (B–E) Temporal evolution of PCR counts within the theta, alpha, beta, and low-gamma bands, respectively. Different colors represent different PCR categories: PCR1 (blue), PCR2 (black), and PCR3 (red). Note the progressive increase in count magnitude from the lower (theta) to higher (low-gamma) frequency bands.

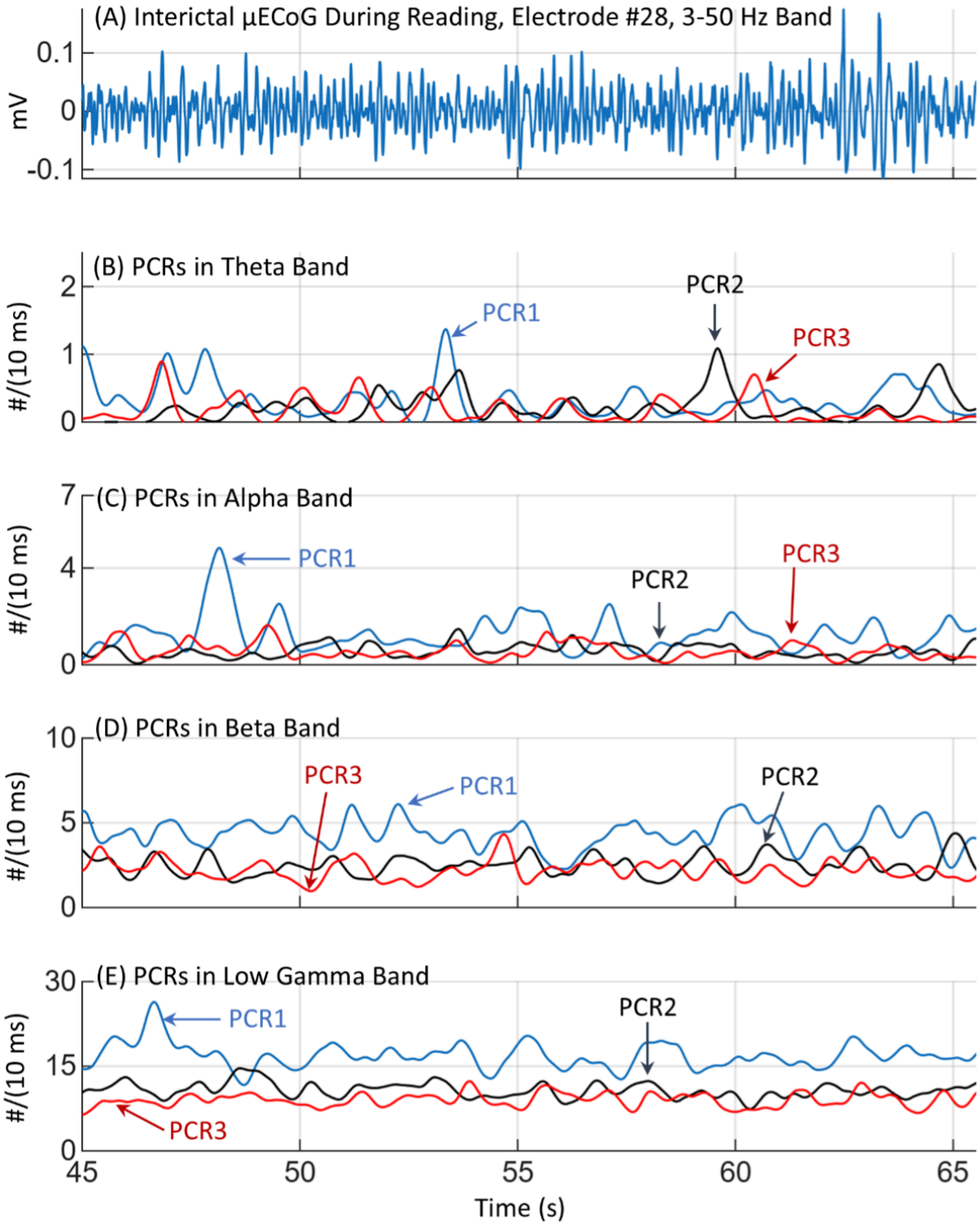


Figure 5

Detailed temporal analysis of PCR fluctuations. Magnified view of the time window from 45 to 65 seconds extracted from Fig. 4. The figure illustrates the high-resolution dynamics and relative peaks of PCR1 (blue), PCR2 (black), and PCR3 (red) across the four frequency bands, demonstrating the coordinated activity across the spectrum during the reading task.